

See discussions, stats, and author profiles for this publication at: <https://www.researchgate.net/publication/260407369>

High-Loading Cobalt Oxide Coupled with Nitrogen-Doped Graphene for Oxygen Reduction in Anion-Exchange-Membrane Alkaline Fuel Cells

DATASET *in* THE JOURNAL OF PHYSICAL CHEMISTRY C · APRIL 2013

Impact Factor: 4.77 · DOI: 10.1021/jp401814f

CITATIONS

61

READS

127

8 AUTHORS, INCLUDING:



Qing Li

Brown University

65 PUBLICATIONS 915 CITATIONS

SEE PROFILE



Samson Khene

Rhodes University

23 PUBLICATIONS 253 CITATIONS

SEE PROFILE



D. Lozano-Castelló

University of Alicante

86 PUBLICATIONS 2,728 CITATIONS

SEE PROFILE

High-Loading Cobalt Oxide Coupled with Nitrogen-Doped Graphene for Oxygen Reduction in Anion-Exchange-Membrane Alkaline Fuel Cells

Qinggong He,^{*,†} Qing Li,[‡] Samson Khene,[§] Xiaoming Ren,^{||} Franz E. López-Suárez,[⊥] Dolores Lozano-Castelló,[⊥] Agustín Bueno-López,[⊥] and Gang Wu^{*,‡}

[†]Department of Molecular & Medical Pharmacology, University of California, Los Angeles, California 90095, United States

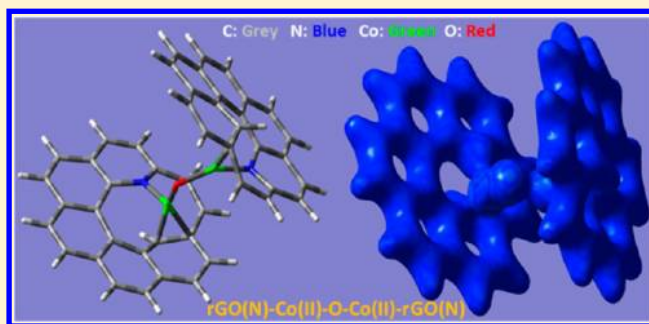
[‡]Materials Physics and Application Division, Los Alamos National Laboratory, Los Alamos, New Mexico 87545, United States

[§]Department of Chemistry, Rhodes University, P.O. Box 94, Grahamstown, 6140, South Africa

^{||}U.S. Army Research Laboratory, Adelphi, Maryland 20783, United States

[⊥]Department of Inorganic Chemistry, University of Alicante, Ap. 99, E-03080, Alicante, Spain

ABSTRACT: A new nanocomposite catalyst consisting of high-loading cobalt oxide (CoO) on nitrogen-doped reduced graphene oxide (rGO) for oxygen reduction reaction (ORR) was prepared in this work. Its high activity for the ORR in alkaline electrolyte was determined using the rotating disk electrode technique, and further confirmed in real alkaline membrane fuel cells. A combination of physicochemical characterization (e.g., X-ray absorption and X-ray photoelectron spectra) and density functional theory (DFT) calculation suggests that cobalt(II) cations in the composite catalyst may coordinate with the pyridinic nitrogen atoms doped into graphene planes, most likely the active species for the ORR. Especially, the DFT calculations indicate that a stable $\text{rGO(N)-Co(II)-O-Co(II)-rGO(N)}$ structure can be formed in the nitrogen-doped graphene catalyst. Kinetic parameter analysis shows a high selectivity of four-electron reduction on the composite catalyst during the ORR with an average electron transfer number of 3.75. A synergistic effect between the rGO(N) and CoO may exist, yielding a much higher catalytic activity on the CoO/rGO(N) catalyst, compared to either rGO(N) or CoO controls. The novel synthesis procedure utilizing rGO(N) to further couple Co(II) yields a high loading of Co species (24.7 wt %). Thus, a relatively thinner cathode in fuel cell can accommodate more active Co species and facilitate O_2 transfer. Due to the high intrinsic activity and efficient mass transport, the CoO-rGO(N) ORR catalyst achieved approaching performance to state-of-the-art Pt/C cathodes in anion-exchange-membrane alkaline fuel cells.



1. INTRODUCTION

Recent progress in anion-exchange membranes (AEM) capable of conducting hydroxide ions (OH^-) as a replacement of liquid electrolytes has revitalized the alkaline fuel cells (AFC) technology and imparted a new momentum to it.^{1–3} Significant attention has been focused on the development of cost-effective catalysts synthesized from earth-abundant elements to substitute the state-of-the-art Pt-based catalysts which are very expensive and poorly tolerant to fuel crossover.^{4,5} As for the oxygen reduction reaction (ORR) at the cathode side of an AFC, a number of non-platinum group metal (PGM) catalysts have shown promising ORR activity in high pH environments, including pyrolyzed transition metal macrocycles,^{6–8} transition-metal-based chalcogenides,^{9–11} and nitrogen-doped carbon materials.^{12,13} In particular, transition-metal (Co or Fe)-based monomeric phthalocyanine and porphyrin systems have been most widely investigated due to their low cost, relatively simple synthesis procedure, and the promising activity comparable to Pt based catalysts.¹⁴ However, there remains some uncertainty

about the active sites of the heat-treated metal- N_4 chelate catalysts adsorbed on carbon, although metal- N_4 moiety,^{15–17} C-N_x functional groups,^{18,19} and $\text{C-N}_x\text{-M}$ ($\text{M} = \text{Co}, \text{Fe}$ or Cu)^{20,21} have been proposed as possible active sites under specific synthesis conditions. Recent $\Delta\mu$ X-ray absorption spectroscopy (XAS) studies have suggested that divacant defective centers (cavities) on the amorphous carbon supports may serve as the anchors for doped nitrogen atoms allowing for coordinating with the central metal atoms.²² In the absence of cavities and doped N on traditional carbon black supports (XC-72, Ketjen black, Black pearl, etc.), metal and metal oxides formed during the thermo-decomposition process are not active for catalyzing the ORR. This result implies that the maximum number of active centers, consisting of metal centers stabilized by nitrogen-containing ligands, is limited by the total

Received: February 20, 2013

Revised: March 25, 2013

Published: April 1, 2013

defect sites of carbon supports. This phenomenon could be the reason for the observation that a maximum in catalytic activity of heat-treated Cl-FeTMPP/C catalysts can only be obtained at a very low metal loading (ca. 2 wt %) after an acidic treatment to remove unstable metal or metal oxides.²³

On the other hand, the currently studied nonprecious metal cathodes for fuel cells are generally very thick (~80–100 μm) in order to provide enough active sites and sustain a large current density.²⁴ However, a thick catalyst layer will lead to a large ohmic resistance and significant mass transport limitations. To increase the number of active sites per unit volume, Lefevre et al. proposed an ideal structure with an active metal cation coordinated by four pyridinic nitrogens in the interstices of two graphitic sheets within the micropores of carbon supports.²⁵ This arrangement of graphite sheets is reminiscent of the structure of graphene. In addition, nitrogen-doped graphene-like structures were observed recently in highly active ORR catalysts.^{26–29} Thus, one would expect to reproduce the possible active site structure by incorporating metal ions into nitrogen-doped graphene. A significant advantage of utilizing graphene or graphene oxide (GO) supports is that much more nitrogen-doped sites containing defective pockets/vacancies are available for coordinating with metal ions, relative to other types of carbon materials. This idea motivated us to prepare a composite catalyst with high-loading transition metal ions onto N-doped GO. In this work, a high metal loading (24.7 wt %) graphene composite catalyst (CoO/rGO(N)) containing much increased active species was prepared using this methodology. Rotating ring disk electrode (RRDE) and fuel cell tests indicated that this high-loading Co-based catalyst behaved comparably to Pt/C for the ORR in alkaline media. The morphology and physicochemical properties of the graphene composite catalysts were extensively characterized to provide insights into the promotional roles of graphene and the possible synergistic effect between the loaded CoO and N-doped graphene.

2. EXPERIMENTAL SECTION

2.1. Materials and Synthesis. Graphene oxide (GO, carbon 79%, oxygen 20%) was purchased from Graphene Supermarket. Ammonia (30% water solution supplied by Panreac) and monohydrate hydrazine (Fluka, purity > 98%) were used as the nitrogen precursor and the reducing agent, respectively. $\text{Co}(\text{NO}_3)_2 \cdot 6\text{H}_2\text{O}$ (Panreac, 98.0%) was used as a cobalt precursor in the catalyst synthesis. To prepare nitrogen-doped GO, the commercial GO was added into water (0.070 g of GO in 35 mL of H_2O) and treated in an ultrasound bath for 1.0 h. The suspension was centrifuged (5 min; 1000 rpm), and the remaining GO in solution was taken from the stable suspension for subsequent synthesis. Ammonia solution was added into the above suspension until a pH of 10 was reached and then 1.0 mL of monohydrate hydrazine was added under constant stirring. The suspension was placed in a stainless steel autoclave with a Teflon liner, and a hydrothermal treatment was carried out at 100 $^\circ\text{C}$ for 3 h. Finally, the suspension was centrifuged (5 min; 1000 rpm) and the solid was washed with deionized water and dried at 40 $^\circ\text{C}$ for 24 h. The overall yield after these reduction and nitrogen doping processes was about 50%. The obtained nitrogen-doped reduced graphene oxide (rGO(N)) was used to couple with cobalt oxide. In doing so, cobalt nitrate was loaded on the rGO(N) by incipient wetness impregnation, and then dried at 40 $^\circ\text{C}$ for 12 h. The cobalt precursor was then decomposed at 220 $^\circ\text{C}$ for 5 h under a N_2

flow (100 mL min^{-1}). The metal content of the CoO/rGO(N) catalyst was determined by ICP-MS [VG Elemental Plasma-quad-2 (PQ2)] around 24.7 wt % Co.

2.2. Physical Characterization. A JEOL (JEM-2010) microscope was used to obtain TEM images of the catalysts. DRIFT spectra were recorded using a JEOL spectrometer (model FT/IR 4100 type A) with a diffuse reflection accessory (Praying Mantis; Harrick Scientific Products, Inc.). X-ray photoelectron spectroscopy (XPS) was carried out in a VG-Microtech Multilab electron spectrometer using an MgK (1253.6 eV) radiation source. The binding energy (BE) and kinetic energy (KE) scales were calibrated using the C 1s transition at 284.6 eV, and the BE and KE values were then determined with the peak-fit software of the spectrometer. The synchrotron-based soft XAS measurements were performed at undulator beamline 8.0.1 at the Advanced Light Source (ALS). The XAS signal was recorded in total electron yield mode (TEY). All data shown are normalized to the incident photon flux monitored by a clean gold mesh. The energy values of the spectra were calibrated by measuring reference samples of Co metals. Raman spectra were recorded in a Bruker RFS 100/S Fourier transform Raman spectrometer with a variable power Nd:YAG laser source (1064 nm). In order to measure the conductivity of the CoO/rGO(N), the powder samples were compressed into pellets under 27 MPa pressure with thicknesses of around several hundred micrometers and bulk densities of around 1.1 g cm^{-2} . Then, its conductivity was measured with a four-point probe electrical measurement setup according to the equation.

$$\sigma \text{ (S m}^{-1}\text{)} = (L_s \times I) / (V \times W_f \times T_f) \quad (1)$$

where L_s is the probe space in m, I is the current in mA, V is the voltage in mV, W_f is the width of the film in m, and T_f is the film thickness in m.

2.3. Computational Methods. The Gaussian 03 program³⁰ running on an Intel/Linux cluster was used to perform DFT calculations. The calculations were done at the B3LYP/6-31G level for geometry optimization. All visualization used the Gausview 4.1 program.³⁰

2.4. Electrochemical Characterization. All electrochemical measurements were carried out at room temperature in a standard three-compartment electrochemical cell using a RRDE setup from Pine Instruments connected to an Autolab (Ecochemie Inc., model-PGSTAT302N) potentiostat. The KOH electrolyte (0.1 M) was prepared using potassium hydroxide pellets (semiconductor grade, 99.99%, Sigma-Aldrich). A glassy carbon electrode (5.61 mm diameter, Pine Instruments) was sequentially polished with 1.0, 0.3, and 0.05 μm alumina paste (Buehler, Lake Bluff, IL) and then sonicated in distilled water for 5 min. Catalyst inks were prepared by dispersing a given amount of catalyst powders in solution containing H_2O :isopropanol (1:1 wt %), followed by a sonication for 1 h. Then, 10 μL aliquots of the catalyst ink were dispensed uniformly on the glassy carbon (GC) disk and dried at room temperature. A Ag/AgCl (3.0 M NaCl) and a graphite rod were used as the reference and counter electrodes, respectively. All potentials are referred to the reversible hydrogen electrode (RHE) unless otherwise stated. In RRDE testing, the ring potential was set to 1.2 V vs RHE. Before experiments, the Pt ring was activated by potential cycling in 0.1 M HClO_4 from 0.0 to 1.4 V vs RHE at a scan rate of 50 mV s^{-1} for 10 min. Four-electron selectivity of catalysts was evaluated on the basis of H_2O^- yields, calculated from eq 2:

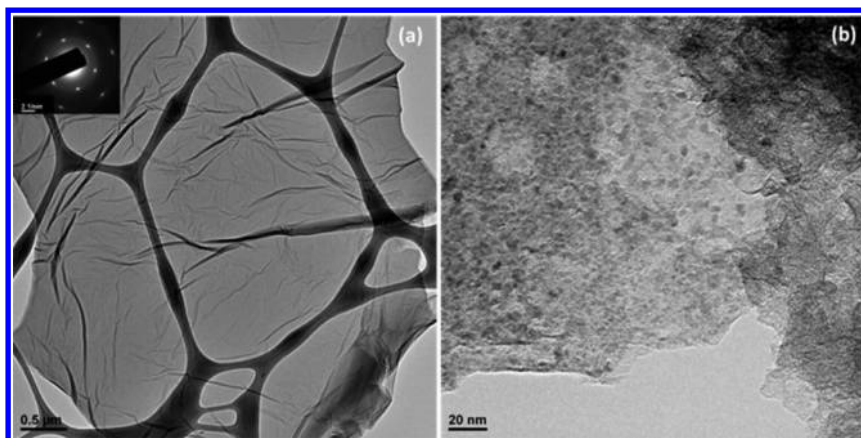


Figure 1. TEM images of the (a) GO and (b) CoO/rGO(N) catalysts.

$$\text{H}_2\text{O}_2 (\%) = 200 \times \frac{I_{\text{R}}/N}{(I_{\text{R}}/N) + I_{\text{D}}} \quad (2)$$

where I_{D} and I_{R} are the disk and ring currents, respectively, and N is the ring collection efficiency (36%).³¹

2.5. Fuel Cell Tests. Fuel cell tests were conducted at the single-cell level with 5 cm² active area electrodes using the standard fuel cell hardware and test station made in Fuel Cell Technology Inc. (Albuquerque, USA). To prepare the fuel cell membrane electrode assembly (MEA), the catalyst ink was formed by mixing the catalyst powder with a 50 vol % isopropanol water solution and the AS4 anion-exchange ionomer (Tokuyama) using an ultrasonic probe. The ionomer content in the dried catalyst ink was controlled at 30 wt %. The anode catalyst ink was uniformly coated onto a hydrophobic carbon cloth backing electrode (A-10 ELAT/NC/V2.02, hydrophobic, E-TEK) to reach a Pt/C catalyst loading of 1.5 mg cm⁻², and the cathode was placed onto a hydrophilic carbon cloth backing electrode (A-10 ELAT/NC/V2.02, hydrophilic, E-TEK) to obtain a loading of 0.75 mg cm⁻². The catalyst layer thickness was estimated to be 7.8 μm for the CoO/rGO(N) cathode and 6.0 μm for the Pt/C cathode. The anion-exchange membrane was pretreated in 0.1 M KOH at room temperature for 24 h, and thoroughly rinsed with deionized water. The MEA was prepared by hot pressing the catalyst coated electrodes onto the A201 Tokuyama membrane at 80 °C under a 2300 kg load for 4 min in a sealed polypropylene bag. The fuel cell tests were conducted at 60 °C with a hydrogen feed (62% RH, 250 cm³/min at 1 atm, 22 °C) at the anode and an oxygen feed (100% RH, 500 cm³/min at 1 atm, 22 °C) at the cathode. Cell voltage–current polarization curves were recorded from a stable open circuit voltage (OCV) followed by each downward step at 25 mV with a waiting time of 60 s.

3. RESULTS AND DISCUSSION

3.1. Catalyst Morphology and Structure. Representative TEM images of the GO and the CoO/rGO(N) catalyst are shown in Figure 1. In the GO image (Figure 1a), a single graphene layer is observed and the selected area electron diffraction (SAED) in the inset shows the typical hexagonal pattern of graphene. The image for CoO/rGO(N) (Figure 1b) shows a region of a graphene sheet covered by well-dispersed nanoparticles with a narrow size distribution of about 1–3 nm,

indicating the loaded cobalt oxide is homogeneously distributed on the rGO.

DRIFT spectra (Figure 2) of GO, rGO(N), and CoO/rGO(N) indicate several types of oxygen-containing functional

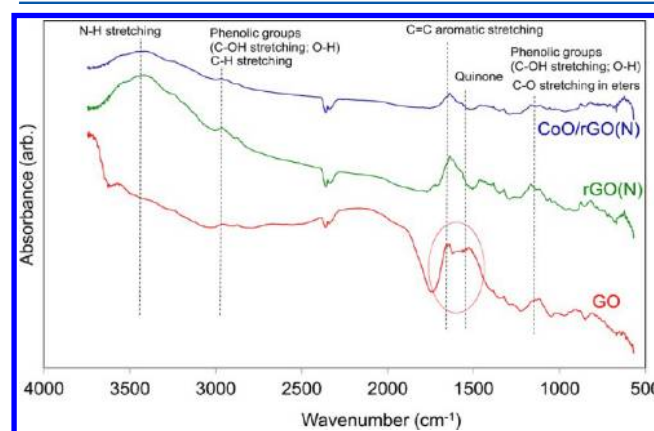


Figure 2. DRIFT spectra of GO, rGO(N), and CoO/rGO(N).

groups in these samples.³² The spectrum of the GO in the circled region is consistent with the presence of different oxygen groups (e.g., phenol, ester, and quinone), and the C=C stretching of aromatic rings is also in evidence. In the cases of rGO(N) and CoO/rGO(N), a wide band at 3400 cm⁻¹ can be assigned to N—H stretching. In addition, some oxygen groups (band at 1500 cm⁻¹) disappear after the hydrothermal treatment in the presence of hydrazine for the nitrogen-doped samples, due to chemical reduction of GO.

The elemental qualification of these samples determined by XPS was summarized in Table 1. As expected, the GO sample contains mostly carbon and oxygen, with a small amount of nitrogen (0.49 at. %). After the hydrothermal treatment in the presence of ammonium and hydrazine, the content of nitrogen in the sample of rGO(N) increases 10 times, relative to the pristine GO, while the oxygen percentage significantly

Table 1. XPS Characterization of the Surface Composition

sample	C (at. %)	N (at. %)	O (at. %)	Co (at. %)
GO	63.53	0.49	33.98	
rGO(N)	82.50	4.36	13.14	
CoO/rGO(N)	72.85	4.03	16.24	6.88

decreases due to the reducing conditions used for nitrogen doping. Subsequent deposition of cobalt species leads to a slight increase in the oxygen content, due to formation of cobalt oxide *via* cobalt nitrate decomposition. The slight decreases in carbon and nitrogen contents are likely from a dilution effect.

Figure 3 shows the N 1s XPS spectra for these three samples. Different types of nitrogen functionalities are distinguished, i.e.,

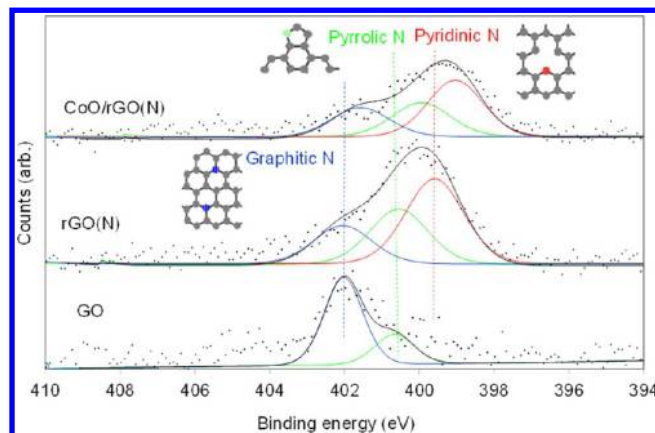


Figure 3. XPS analysis of N1s of GO, rGO(N), and CoO/rGO(N).

N at the edges of the graphene layers in six-membered rings (pyridinic nitrogen), N in five-membered rings (pyrrolic nitrogen), and N in six-membered rings within the graphene layers (graphitic nitrogen). The GO sample has small amounts of graphitic and pyrrolic nitrogen. As for the rGO(N) sample, incorporated nitrogen atoms during the hydrothermal treatment with hydrazine and ammonia are mainly in a pyridinic form.^{33–35} The shift in the position of the N peaks toward lower binding energies upon cobalt loading could be indicative of electron transfers between the transition metal and nitrogen groups due to their possible coordination. This is consistent with the Pauling electronegativity values, being 3.0 for N and 1.8 for Co. As N is more electronegative, electron density will be transferred from Co to N. It has been reported that the interaction of Co or Fe ions with N in porphyrins leads to a lower N binding energy of about 399.2 eV,^{36–38} which is in good agreement with the energy of the most intense peak observed with the CoO/rGO(N) sample.

Figure 4 shows the Co 2p XPS spectra, where the Co 2p_{3/2} and Co 2p_{1/2} components are distinguished along with two

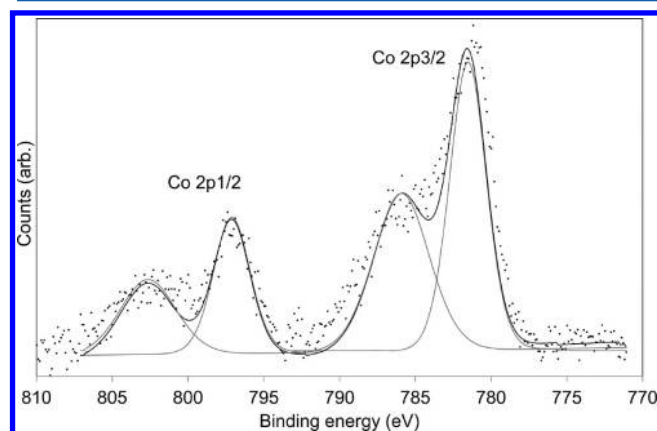


Figure 4. XPS analysis of Co 2p for the CoO/rGO(N) sample.

satellite peaks. The Co 2p_{3/2} and Co 2p_{1/2} peaks, located at binding energies of 781.6 and 796.8 eV, respectively, are the typical characteristics of Co²⁺ species.³⁹ These peaks may be attributed to the presence of CoO and/or Co(OH)₂. The presence of metal cobalt can be eliminated or its content is below the detectable limits, because of the absence of peak at 778 eV.⁴⁰ Thus, the dominant Co species on the CoO/rGO(N) catalyst exists in the form of Co(II) cation.

In order to further identify the structural information of the CoO/rGO(N) catalyst, XAS measurements were conducted on the Co L-edge and N K-edge, as shown in Figure 5a and b,

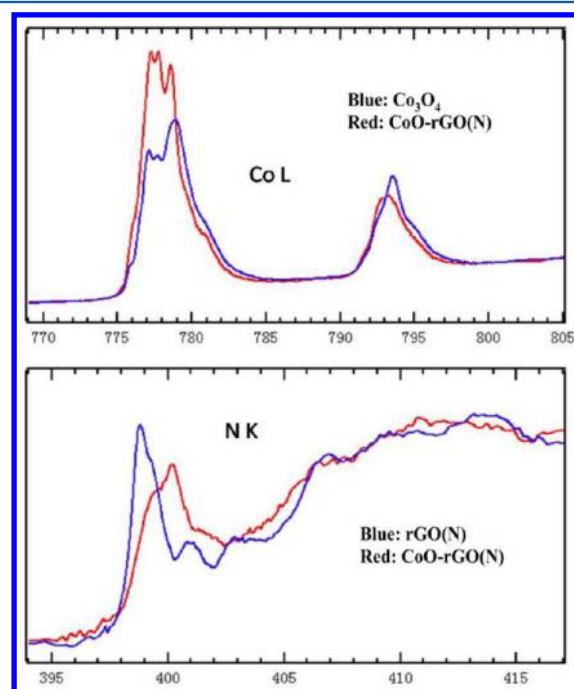


Figure 5. (a) Co L-edge XAS, experimental spectra of Co₃O₄ (blue) and CoO-rGO(N) (red). (b) N K-edge XAS, experimental spectra of rGO(N) (blue) and CoO-rGO(N) (red).

respectively. It is known that XAS spectra correspond to the unoccupied density of states in the conduction band of the material.⁷ In a standard reference of Co₃O₄, Co³⁺ is octahedrally coordinated and Co²⁺ is tetrahedrally coordinated with oxygen, where Co³⁺/Co²⁺ = 2:1.⁴¹ Compared to the Co₃O₄, the Co L-edge absorption features of CoO/rGO(N) have moved to lower energy and a decrease in the ratio of high-energy peak (778.9 eV) to low-energy peak (777.6 eV) has been observed, indicating the valence of the Co remains 2+ dominantly. Importantly, the Co-L edge data of CoO/rGO(N) match the rock salt CoO structure with the octahedrally coordinated Co²⁺ state.^{41,42} The possible interactions between N and Co atoms can be further supported by XAS data at the N K-edge (Figure 5b). According to the literature,^{43,44} the peaks at 398.1 eV for pyridinic N, ~400 eV for pyrrolic N, and 401.0 eV for graphitic N are features corresponding to N (1s) → π^* transitions. As compared to rGO(N), the features related to N move to higher energy after loading CoO. It indicates that the content of pyridinic N (and pyrrolic N, if any) is reduced. The possible explanation is that the formation of N–Co coordination reduces pyridinic N functionalities. The electronic unsaturated and steric accessible pyridinic N or pyrrolic N offers more feasibility and convenience for such coupling.

Figure 6 compares the Raman spectra for different samples, presenting features typical of carbon materials with several

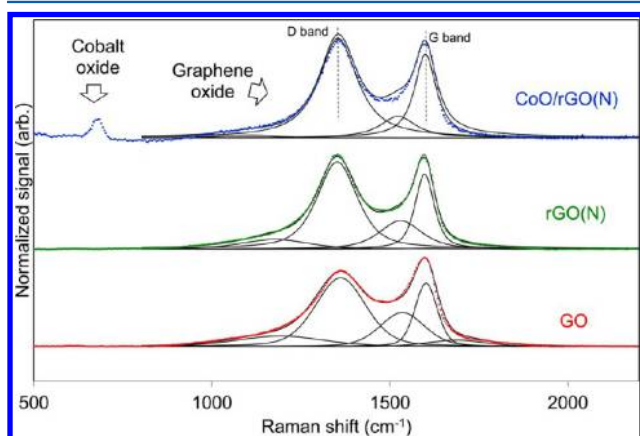
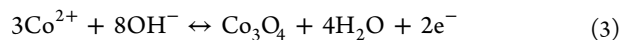


Figure 6. Raman spectra of GO, rGO(N), and CoO/rGO(N).

bands in a range of 100–1800 cm^{-1} . The CoO/rGO(N) catalyst shows an additional cobalt oxide peak at 672 cm^{-1} .^{45,46} The carbon fingerprint, which has been deconvoluted into several contributions, presents two main peaks referred to as G and D bands.⁴⁷ The G band at 1590 cm^{-1} corresponds to the “in-plane” displacement of carbon atoms strongly coupled in hexagonal sheets. This is an ideal graphitic lattice vibration mode with E_{2g} symmetry, and thereby characterizes the highly ordered graphite carbon materials. The D band (or “defect” band) at 1352 cm^{-1} is the characteristic of disordered graphite and corresponds to a graphitic lattice vibration mode with A_{1g} symmetry. In addition, some other minor bands complete the deconvoluted profiles, such as a band at 1520 cm^{-1} , which is associated with distortion, five-sided ring, and heteroatom doping. The small band at 1200 cm^{-1} can be attributed to sp^2 carbon atoms outside the graphene network. The D/G intensity ratio is an index of the disorder degree and the average size of the sp^2 domains. The D/G intensity ratio decreases slightly from 1.2 for GO to 0.97 and 0.93 for the rGO(N) and CoO/rGO(N) samples, respectively, thereby providing evidence that the graphene structure is essentially restored upon the chemical reducing.

3.2. Catalyst ORR Activity and Electrochemical Properties. Figure 7 compares the CVs of CoO/rGO(N) and other control samples in Ar-saturated 0.1 M KOH solution at a sweep rate of 10 mV s^{-1} . The rGO exhibits no surface redox-related peaks except for the capacitive current. This is due to the fact that effective chemical reduction leads to a complete removal of oxygen-containing functionalities from the GO. However, subsequent nitrogen-doping results in a cathodic peak at 0.73 V related to the formation of $\text{C}-\text{N}$ or $\text{C}=\text{N}$ or amide bonds,⁴⁸ while the corresponding anodic peak at 0.82 V was submerged in the capacitive current. On the other hand, the free-standing CoO sample starts oxidizing at 1.0 V and shows an obvious redox couple around 1.3 V . The possible electrochemical reactions could be assigned to¹³



In the CV of the CoO/rGO(N) composite catalyst, metal oxide redox peaks are not superimposed on a capacitive current from the rGO(N) support due to the high metal loading in the

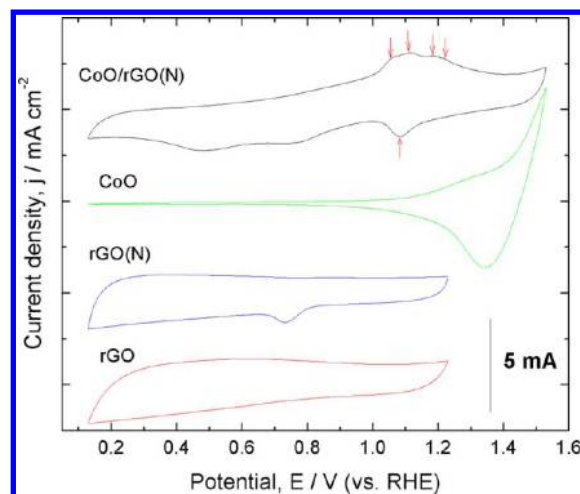


Figure 7. Cyclic voltammograms for the CoO/rGO(N) catalyst and other controls (CoO, rGO, and rGO(N) in 0.1 M KOH at $25\text{ }^\circ\text{C}$; catalyst loading 0.6 mg cm^{-2} , scan rate 10 mV s^{-1}).

catalyst (27.4 wt %). Dominant redox peaks (indicated by arrows) are clearly associated with the oxidation of Co(II) species, as shown in eqs 3 and 4. These peaks imply that a large amount of Co(II) species are present on the catalyst surface. Given the possible coordination between Co and doped N, the redox can be schematically expressed as eq 5.



It is worth noting that a broad anodic peak around 1.1 V can be split into four small ones indicated by the arrows. This may be due to the difference in binding energies among Co and pyrrolic/pyridinic N as well as the $\text{Co}-\text{O}$ binding in CoO species.

ORR activity and four-electron selectivity (peroxide yield) data for the CoO/rGO(N) catalyst and other controls including CoO, rGO, CoO/rGO, rGO(N), and Pt/C catalysts are shown in Figure 8. Both CoO and rGO samples exhibit poor ORR activity and suffer from a high yield of peroxide. This suggests that activity of CoO or rGO is insufficient to effectively catalyze oxygen reduction. While the incorporation of CoO onto rGO can reduce the peroxide yield to ca. 13%, the ORR activity of CoO/rGO is still insufficient. In the case of the rGO(N), the introduction of nitrogen leads to an obvious improvement in activity, evidenced by the positive shifts of the onset ORR potential and the half-wave potential ($E_{1/2}$)^{49,50} to 0.85 and 0.75 V vs RHE, respectively. However, the peroxide yield still remains very high around 10%. It has been indicated that, theoretically and experimentally, nitrogen can be viewed as an n-type dopant into graphene forming disordered nanostructures and donating more electrons, as the two possible ways to facilitate oxygen reduction in carbonaceous materials. However, such active sites appear unable to effectively reduce oxygen to OH^- through a four-electron route. The simultaneous additions of nitrogen and CoO species into the rGO(N) for the CoO/rGO(N) catalyst dramatically improve the ORR activity and four-electron selectivity. The measured ORR onset and $E_{1/2}$ potentials with the CoO/rGO(N) catalyst are as high as 0.95 and 0.83 V , respectively. Relative to cobalt oxide/graphene or N-doped graphene ORR catalysts reported by other groups,^{12,51,52} the catalyst in this work was developed by a different synthesis route and reveals comparable or even higher ORR activity. For example, the $E_{1/2}$ measured with the CoO/

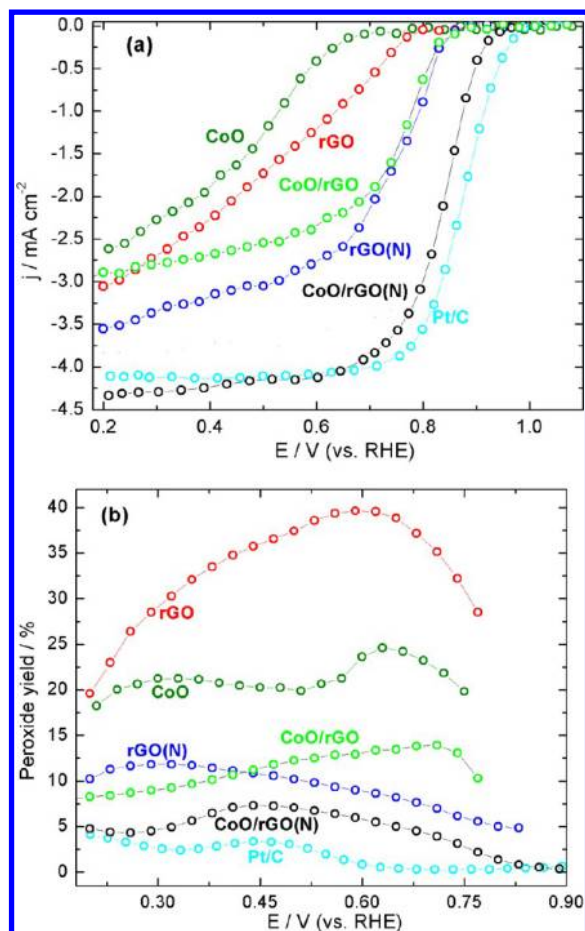


Figure 8. Steady-state polarization plots for ORR on the CoO/rGO(N) catalyst and other controls (CoO, rGO, rGO(N), Pt/C): (a) RDE activity and (b) peroxide yield in 0.1 M O_2 -saturated KOH at 25 °C and 900 rpm; non-Pt catalyst loading 0.6 mg cm^{-2} ; Pt/C loading $20 \text{ } \mu\text{g (Pt) cm}^{-2}$.

rGO(N) is comparable with other graphene-based catalysts, such as Co_3O_4 /nitrogen-doped reduced mild graphene oxide (N-rmGO)⁵¹ ($\sim 0.82 \text{ V}$), CoO/carbon nanotubes⁴³ ($\sim 0.83 \text{ V}$), MnCo_2O_4 /N-rmGO⁵² ($\sim 0.82 \text{ V}$), and $\text{Co}_{1-x}\text{S}/\text{RGO}$ ⁵³ ($\sim 0.78 \text{ V}$) reported by Dai's group. Furthermore, the catalyst is able to offer better ORR activity than Fe-based graphene catalysts, such as nitrogen-doped graphene (NG)/Fe⁵⁴ ($\sim 0.71 \text{ V}$) and Fe_3O_4 /NG⁵⁵ ($\sim 0.51 \text{ V}$) developed by Müllen's group. Our catalyst also outperforms some other graphene materials including nitrogen-doped graphene⁵⁶ ($E_{1/2} = \sim 0.51 \text{ V}$) and Co/CoO-graphene¹² ($E_{1/2} = \sim 0.70 \text{ V}$). The determined peroxide yield has been reduced to 5% at 0.20 V. Noteworthy, a well-defined current density plateau controlled by mass transfer, following the charge-transfer kinetics control potential range, was observed for the CoO/rGO(N) sample, attesting to the high density and uniform distribution of ORR active sites on the catalyst.⁵⁷ The activity gap between the state-of-the-art Pt/C (E-TEK) and the CoO/rGO(N), expressed as a difference of half-wave potential ($\Delta E_{1/2}$) in rotating disk electrode (RDE) testing, has been substantially reduced to 20 mV (0.85 vs 0.83 V). Measured peroxide yields of the Pt/C and CoO/rGO(N) catalysts were also comparable. The role of Co species in active ORR sites has been the subject of an ongoing debate. In this work, the coordinated Co(II) and pyridinic/pyrrolic N

evidenced by XAS and XPS analysis are likely the active species dispersed onto the rGO surface for the ORR.

Hydrodynamic RDE voltammograms of the CoO/rGO(N) electrode in O_2 -saturated 0.1 M KOH are displayed in Figure 9a. In these plots, three separate potential regions can be

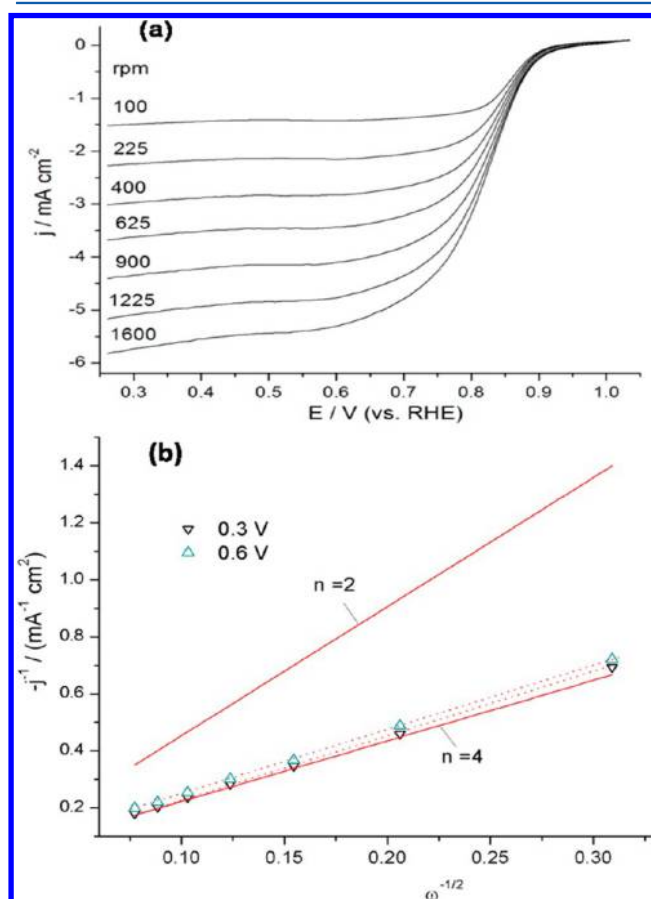


Figure 9. (a) RDE polarization plots obtained with different rotation rates. (b) Koutecky–Levich plots for ORR in O_2 -saturated 0.1 M KOH on CoO/rGO(N) catalysts; scan rate 10 mV s^{-1} .

identified. At high potentials ($E > 0.85 \text{ V}$), the ORR is under kinetic control. This is followed by a mixed diffusion-kinetic limited region ($0.6\text{--}0.85 \text{ V}$). At low potentials ($E < 0.6 \text{ V}$), the ORR is controlled purely by O_2 diffusion.

The Koutecky–Levich (K–L, $1/j$ vs $1/\omega^{1/2}$) plots obtained from ORR polarization curves at different rotation speeds are presented in Figure 9b for the CoO/rGO(N) electrode.

In Figure 9b, good linear fitting can be seen for each potential with the identical slopes. The calculated electron transfer number for the CoO/rGO(N) electrode is 3.75. This result is in good agreement with the peroxide yield determined by RRDE tests. Thus, the composite catalyst is able to reduce O_2 to OH^- in alkaline media mostly through a direct four-electron or a two + two route in the regions controlled by mass diffusion and mixed kinetic diffusion. It has been determined that cobalt oxide tends to produce a significant amount of HO_2^- with the $n = 2$ during ORR in alkaline media.^{58,59} Therefore, the much improved ORR performance observed with the composite catalyst suggested that cobalt species are likely embedded in the N-doped graphene framework and coordinate with nitrogen functionalities, rather than stand alone CoO.

Figure 10 shows representative Tafel plots of ORR for the CoO/rGO(N) catalyst and other controls. Kinetic current

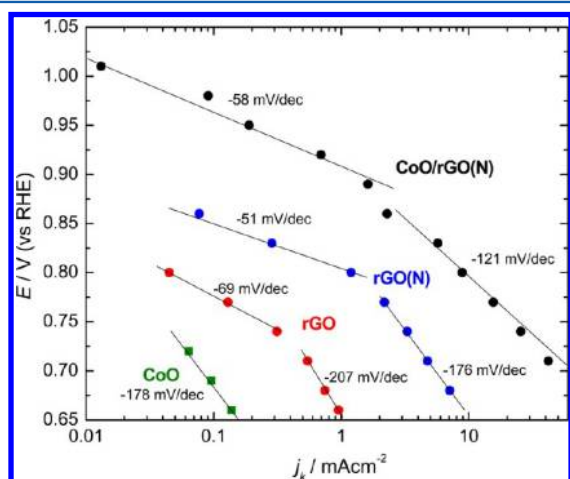


Figure 10. Tafel plots for the ORR on the CoO/rGO(N) catalyst and other controls.

densities extracted from the steady-state polarization according to the K–L equation were used to plot these Tafel plots.⁶⁰

Similar to Pt catalysts for ORR in alkaline media,⁶¹ two Tafel regions can be defined for the CoO/rGO(N) catalyst. Tafel slopes transit from -58 mV dec^{-1} ($E > 0.87 \text{ V}$) to -121 mV dec^{-1} ($E < 0.87 \text{ V}$). In general, oxygen reduction in aqueous alkaline media is a complicated electrocatalytic reaction.^{62,63} Many species have been proposed as intermediates in this multistep reaction, including O, OH, O_2^- , and HO_2^- , leading to a great number of possible mechanisms. Similar Tafel slopes

once were observed on Pt electrodes in alkaline media by Damjanovic and co-workers.⁶¹ Theoretically, a Tafel slope of -118 mV dec^{-1} is due to the rate-determining step associated with the first electron transfer leading to approximate Langmuirian adsorption, while a Tafel slope around -59 mV dec^{-1} had been ascribed to the coverage of adsorbed oxygen, with a Temkin adsorption of O at higher coverage of oxide or adsorbed oxygen intermediates, leading to a coverage-dependent activation barrier for electrochemical reactions.^{64–66} It is worth noting that the rGO and rGO(N) also exhibit a similar Tafel slope close to -59 mV dec^{-1} at the high potential ranges, suggesting migration of adsorbed oxygen intermediates limits the ORR. However, the Tafel slopes measured with these control samples at the low potential range exhibit high values ranging from -170 to -210 mV dec^{-1} . Such higher Tafel slope in the high current densities region may be related to a change in the rate-determining step. One of the possibilities, presented for the first time by Tarasevich,⁶⁷ for explanation of the high Tafel slopes ($200\text{--}300 \text{ mV dec}^{-1}$) for ORR on Pt and Pt group metals implies adsorption of molecular oxygen as the rate-determining step of ORR.⁶⁷

3.3. DFT Results. DFT calculations were carried out to elucidate the nature of the interaction between CoO and pyridinic N. Figure 11a shows an optimized structure of GO(N)–Co(II)–O–Co(II)–GO(N) with pyridinic N interacting with CoO. The structure was chosen on the basis of experimental results, which suggests that the CoO/rGO(N) sample consists mainly of pyridinic N after the hydrothermal treatment. In Figure 11, the bonds between carbon and cobalt are generated during the calculations. This is possible, since it is known that defect site carbons, on graphite, are highly reactive. Parts b, c, and d of Figure 11 show the highest occupied

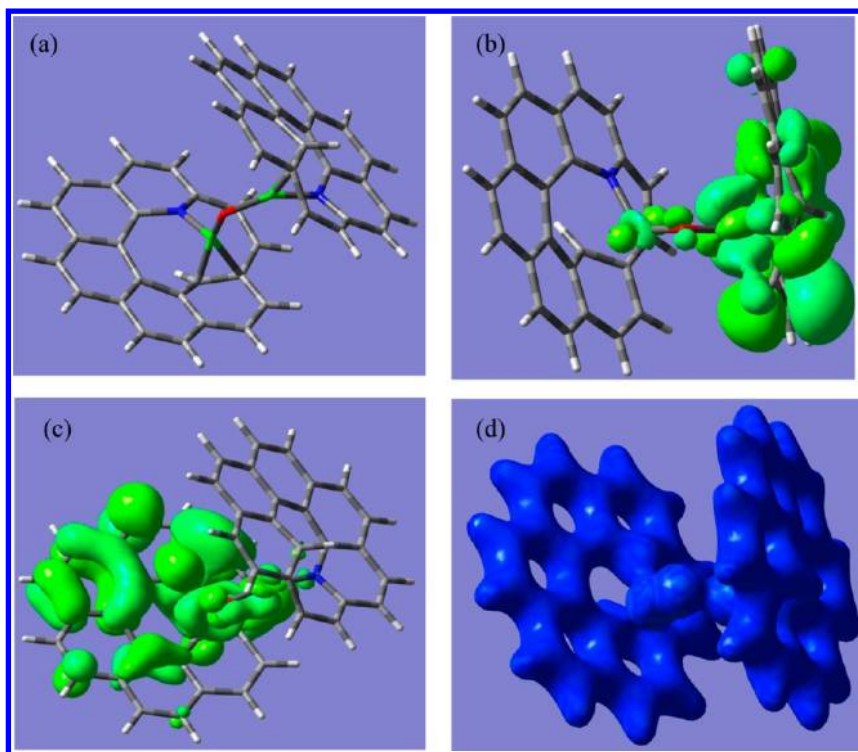


Figure 11. Optimized structure (a), highest occupied molecular orbital (HOMO) (b), lowest unoccupied molecular orbital (c), and electron density map (d) of rGO(N)–Co(II)–O–Co(II)–rGO(N). The structure was optimized at the B3LYP/6-31G level of theory. Carbon (gray), nitrogen (blue), cobalt (green), and oxygen (red).

molecular orbital (HOMO), the lowest unoccupied molecular orbital (LUMO), and the electron density map, respectively. Figure 11b shows an unsymmetrical distribution of orbitals on the GO(N)–Co(II)–O–Co(II)–GO(N) structure. However, the excited state (Figure 11c) shows a different molecular orbital (MO) distribution pattern. The MO is now delocalized on a different side of the GO(N)–Co(II)–O–Co(II)–GO(N) structure (Figure 11c). The bonding orbital between the cobalt, nitrogen, and the defect site carbon atoms is clearly observed. This observation suggests that a covalent bond is formed between the cobalt, nitrogen, and defect site carbon atoms. The electron density map, Figure 11d, also shows an electron density distribution around cobalt, nitrogen, and defect site carbon atoms. However, experimental results suggest that cobalt remains in the +2 oxidation state. The bonding orbital observed between the cobalt and the defect site carbon atoms indicates that there is coordination between cobalt and the defect site carbons. Direct coordination of transition metal, such as Cu(II), to single wall carbon nanotubes is known.⁶⁸ Due to the bonding and coordination observed between cobalt, nitrogen, and the defect site carbon atoms, addition of CoO may result in a reduction of the number of defect sites for pyridinic GO(N). Thus, the reduction in defect sites suggests that cobalt will play a greater role in electrocatalytic reduction of O₂ to OH[−], compared to defect sites in rGO(N). This observation further supports the experimental results discussed above, attesting that cobalt is involved in active sites for the ORR. It is well-known that catalytic properties inherent in the partially filled orbitals of the transition metal ions can be much enhanced when chelated by porphyrins or their derivatives.⁶⁹ Figure 11b shows extensive molecular orbital delocalization on the cobalt atom, which could serve as a viable active site for O₂ adsorption. In this work, it is possible that the catalytic properties of cobalt toward ORR are enhanced due to the binding of the pyridinic nitrogen and coordination of defect site carbon atoms to the cobalt.

3.4. Anion-Exchange-Membrane Alkaline Fuel Cells.

The ORR catalytic performance of the CoO/rGO(N) catalyst was further evaluated in a real H₂/O₂ alkaline fuel cell and compared to the Pt/C cathode under identical cell operating conditions. The voltage–current polarization curves measured at 60 °C for both CoO/rGO(N) and Pt cathodes are shown in Figure 12.

Compared to the Pt/C cathode, the cell with the CoO/rGO(N) cathode only has a slightly decreased OCV around 38 mV. A similar downward voltage shift at the low current density range was observed for the CoO/rGO(N) cathode. This downward shift is in agreement with the observed low kinetic current measured from the RDE experiments for these two catalysts. In particular, at a cell voltage of 0.6 V, the current densities obtained with the Pt/C and CoO/rGO(N) cathodes are 430 and 320 mA cm^{−2}, respectively, corresponding to respective power densities of 260 and 190 mW cm^{−2}. Due to the relatively high energy conversion efficiency, the typical operating voltages in fuel cells are around 0.6 V.⁷⁰ Hence, the power outcome of the precious-metal-free CoO/rGO(N) catalyst is closely approaching that of the Pt catalysts in these practical voltages. Still, the maximum power densities reached by the cells with the CoO/rGO(N) cathode are lower than those with the Pt/C cathode (248 vs 387 mW cm^{−2}). The larger voltage drop at the high current density range for the CoO/rGO(N) cathode can be largely attributed to its relatively low electron conductivity, compared to Pt/C. In this work, we

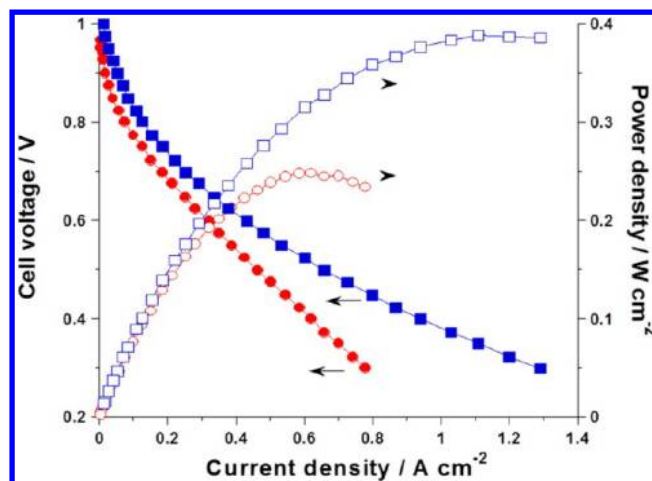


Figure 12. Performance of anion-exchange-membrane fuel cells using identical Pt/C anodes with Pt/C (square symbols) and CoO/rGO(N) cathodes (circle symbols) tested at 60 °C with H₂ (at 1 atm, 57% RH) feed at the anode and O₂ (at 1 atm, 100% RH) at the cathode. The cell voltage–current polarization curves (filled symbols) on the left axis and the power current curves (open symbols) on the right axis.

measured the electron conductivity of samples as a function of synthesis step. Actually, the pristine GO is an insulator with a low conductivity of around 0.5 S m^{−1}. The 3 orders of magnitude increase in conductivity was obtained with the rGO (0.4 × 10³ S m^{−1}) by the deoxygenation and dehydration. Subsequent nitrogen doping leads to a further improvement in conductivity to 1.1 × 10³ S m^{−1}. However, deposition of CoO onto the reduced rGO(N) results in a decrease of conductivity to 5.1 × 10² S m^{−1} measured with the CoO/rGO(N) samples. Thus, further enhancement of electron conductivity in the composite catalyst is still needed by optimizing the ratio of CoO and rGO as well as the chemical and physical properties of rGO with high conductivity.

An extended life test for the cell with the CoO/rGO(N) cathode at a constant cell voltage of 0.6 V over 240 h was carried out, and 50% performance loss was observed. However, a comparable loss has also been observed for the Pt/C cathode. Importantly, it was found that the decline was accompanied by an increase in cell ionic resistance, indicating the gradual loss of hydroxide ions in the membrane is likely the main reason for the performance degradation. CO₂ permeation from ambient air into the cell test chamber was found to be the primary cause for the rapid decrease in the membrane hydroxide conductivity observed during the life test. With pressurized H₂ and O₂ gas stream feeding to the fuel cell during the life tests, we observed that the stability of the membrane conductivity and fuel cell performance can be improved. Other possible causes of the cell performance loss could be attributed to the poor stability of the anion exchanging ionomer used because of its excessive degree of water uptake at elevated temperature. Thus, with the current available ionomer materials, the decrease in the anion-exchange-membrane fuel cell performance could not be unambiguously assigned to the catalyst stability.

4. CONCLUSIONS

A novel graphene nanocomposite catalyst containing high-loading cobalt oxide (24.7 wt %, Co) was developed in this work *via* incorporating CoO onto nitrogen-doped reduced graphene oxide. During the catalyst synthesis, nitrogen was

doped into reduced GO before the incorporation of CoO. This method may enhance the efficiency of nitrogen doping compared with other methods to prepare nitrogen-doped graphene catalysts,⁵¹ in which the metal precursor, nitrogen source, and GO are mixed together. In addition, compared to other nitrogen-doped GO^{54,56} generated from heat treatment up to 1000 °C, the newly developed method is more facile and the catalyst yield is higher.

The Co(II) is identified as a dominant cobalt species on catalysts, and most likely coordinately coupled with pyridinic N doped into graphene planes, evidenced by X-ray absorption spectra and DFT calculations. In particular, DFT calculations suggest that CoO can strongly couple with pyridinic nitrogens in the rGO(N) and thus form a stable structure represented as rGO(N)–Co(II)–O–Co(II)–rGO(N). The D-to-G band ratios determined in the Raman spectra suggest that addition of CoO may decrease the degree of defected carbons in GO, further strengthening the interaction between CoO species and graphene. With this unique structure, a synergistic effect between rGO(N) and cobalt oxide may facilitate the ORR in alkaline media, yielding a much improved activity and four-electron selectivity, when compared to either rGO(N) or CoO. Importantly, due to the richness of defects and nitrogen doping, the graphene-based supports can accommodate a high Co loading, leading to a thin cathode layer with enhanced mass transfer in alkaline fuel cells.

Importantly, we demonstrated the real activity of the CoO/rGO(N) cathode in a real alkaline anion-exchange-membrane fuel cell, showing approaching performance to state-of-the-art Pt/C catalysts. Optimizations of the CoO-to-GO ratios in catalysts as well as the procedures for GO reduction and nitrogen doping are still needed to further improve the catalyst performance.

AUTHOR INFORMATION

Corresponding Author

*E-mail: QHe@mednet.ucla.edu (Q.H.); wugang@lanl.gov (G.W.). Phone: (+1) 510-542-1147 (Q.H.); (+1) 505-665-0659 (G.W.).

Notes

The authors declare no competing financial interest.

ACKNOWLEDGMENTS

We would like to thank B. Shyam and F. McLarnon for helpful comments and suggestions during preparation of this manuscript. The financial support from the Los Alamos National Laboratory Early Career Laboratory-Directed Research and Development (LDRD) Program for this work is gratefully acknowledged.

REFERENCES

- (1) Slade, R. C. T. Alkaline Anion-Exchange Membrane Fuel Cells (AMFCs). *Abs. Papers, 234th ACS National Meeting, Boston, MA, United States, August 19–23, 2007*, FUEL-042.
- (2) Slade, R. C. T.; Varcoe, J. R. Alkaline Anion-Exchange Membrane Fuel Cells (AMFCs). *Prepr. Symp. - Am. Chem. Soc., Div. Fuel Chem.* **2007**, 52, 319–320.
- (3) Varcoe, J. R.; Slade, R. C. T. An Electron-Beam-Grafted Etfe Alkaline Anion-Exchange Membrane in Metal-Cation-Free Solid-State Alkaline Fuel Cells. *Electrochem. Commun.* **2006**, 8, 839–843.
- (4) He, D. P.; Jiang, Y. L.; Lv, H. F.; Pan, M.; Mu, S. C. Nitrogen-Doped Reduced Graphene Oxide Supports for Noble Metal Catalysts

with Greatly Enhanced Activity and Stability. *Appl. Catal., B* **2013**, 132–133, 379–388.

- (5) Vinayan, B. P.; Nagar, R.; Rajalakshmi, N.; Ramaprabhu, S. Novel Platinum-Cobalt Alloy Nanoparticles Dispersed on Nitrogen-Doped Graphene as a Cathode Electrocatalyst for Pemfc Applications. *Adv. Funct. Mater.* **2012**, 22, 3519–3526.

- (6) Wang, B. Recent Development of Non-Platinum Catalysts for Oxygen Reduction Reaction. *J. Power Sources* **2005**, 152, 1–15.

- (7) He, Q.; Yang, X.; He, R.; Bueno-Lopez, A.; Miller, H.; Ren, X.; Yang, W.; Koel, B. E. Electrochemical and Spectroscopic Study of Novel Cu and Fe-Based Catalysts for Oxygen Reduction in Alkaline Media. *J. Power Sources* **2012**, 213, 169–179.

- (8) He, Q.; Yang, X.; Ren, X.; Koel, B. E.; Ramaswamy, N.; Mukerjee, S.; Kostecki, R. A Novel CuFe-Based Catalyst for the Oxygen Reduction Reaction in Alkaline Media. *J. Power Sources* **2011**, 196, 7404–7410.

- (9) Alonso-Vante, N. Structure and Reactivity of Transition Metal Chalcogenides toward the Molecular Oxygen Reduction Reaction. *Mod. Aspects Electrochem.* **2011**, 51, 255–300.

- (10) Tritsarlis, G. A.; Norskov, J. K.; Rossmeisl, J. Trends in Oxygen Reduction and Methanol Activation on Transition Metal Chalcogenides. *Electrochim. Acta* **2011**, 56, 9783–9788.

- (11) Wu, G.; Cui, G.; Li, D.; Shen, P.-K.; Li, N. Carbon-Supported Co_{1.67}Te₂ Nanoparticles as Electrocatalysts for Oxygen Reduction Reaction in Alkaline Electrolyte. *J. Mater. Chem.* **2009**, 19, 6581–6589.

- (12) Guo, S. J.; Zhang, S.; Wu, L. H.; Sun, S. H. Co/CoO Nanoparticles Assembled on Graphene for Electrochemical Reduction of Oxygen. *Angew. Chem., Int. Ed.* **2012**, 51, 11770–11773.

- (13) Liang, Y.; Wang, H.; Diao, P.; Chang, W.; Hong, G.; Li, Y.; Gong, M.; Xie, L.; Zhou, J.; Wang, J.; et al. Oxygen Reduction Electrocatalyst Based on Strongly Coupled Cobalt Oxide Nanocrystals and Carbon Nanotubes. *J. Am. Chem. Soc.* **2012**, 134, 15849–15857.

- (14) Zhang, L.; Zhang, J.; Wilkinson, D. P.; Wang, H. Progress in Preparation of Non-Noble Electrocatalysts for Pem Fuel Cell Reactions. *J. Power Sources* **2006**, 156, 171–182.

- (15) Bouwkamp-Wijnoltz, A. L.; Visscher, W.; van Veen, J. A. R.; Boellaard, E.; van der Kraan, A. M.; Tang, S. C. On Active-Site Heterogeneity in Pyrolyzed Carbon-Supported Iron Porphyrin Catalysts for the Electrochemical Reduction of Oxygen: An in Situ Moessbauer Study. *J. Phys. Chem. B* **2002**, 106, 12993–13001.

- (16) Van Veen, J. A. R.; Colijn, H. A.; Van Baar, J. F. On the Effect of a Heat Treatment on the Structure of Carbon-Supported Metalloporphyrins and Phthalocyanines. *Electrochim. Acta* **1988**, 33, 801–804.

- (17) Van Veen, J. A. R.; Van Baar, J. F.; Kroese, K. J. Effect of Heat Treatment on the Performance of Carbon-Supported Transition Metal Chelates in the Electrochemical Reduction of Oxygen. *J. Chem. Soc., Faraday Trans. 1* **1981**, 77, 2827–2843.

- (18) Wiesener, K. N₄-Chelates as Electrocatalyst for Cathodic Oxygen Reduction. *Electrochim. Acta* **1986**, 31, 1073–1078.

- (19) Franke, R.; Ohms, D.; Wiesener, K. Investigation of the Influence of Thermal Treatment on the Properties of Carbon Materials Modified by Nitrogen (N₄)-Chelates for the Reduction of Oxygen in Acidic Media. *J. Electroanal. Chem. Interfacial Electrochem.* **1989**, 260, 63–73.

- (20) Tanaka, A.; Gupta, S. L.; Tryk, D.; Fierro, C.; Yeager, E. B.; Scherson, D. A. Electrochemical and Spectroscopic Aspects of Heat-Treated Transition Metal Macrocycles as Electrocatalysts for Oxygen Reduction. *Proc. - Electrochem. Soc.* **1992**, 92–11, 555–572.

- (21) Scherson, D. A.; Gupta, S. L.; Fierro, C.; Yeager, E. B.; Kordesch, M. E.; Eldridge, J.; Hoffman, R. W.; Blue, J. Cobalt Tetramethoxyphenyl Porphyrin. Emission Moessbauer Spectroscopy and Oxygen Reduction Electrochemical Studies. *Electrochim. Acta* **1983**, 28, 1205–1209.

- (22) Ramaswamy, N.; Mukerjee, S. Fundamental Mechanistic Understanding of Electrocatalysis of Oxygen Reduction on Pt and Non-Pt Surfaces: Acid Versus Alkaline Media. *Adv. Phys. Chem.* **2012**, 491604–491617.

- (23) Lefevre, M.; Dodelet, J. P.; Bertrand, P. O₂ Reduction in Pem Fuel Cells: Activity and Active Site Structural Information for Catalysts Obtained by the Pyrolysis at High Temperature of Fe Precursors. *J. Phys. Chem. B* **2000**, *104*, 11238–11247.
- (24) Nallathambi, V.; Lee, J. W.; Kumaraguru, S. P.; Wu, G.; Popov, B. N. Development of High Performance Carbon Composite Catalyst for Oxygen Reduction Reaction in PEM Proton Exchange Membrane Fuel Cells. *J. Power Sources* **2008**, *183*, 34–42.
- (25) Lefevre, M.; Proietti, E.; Jaouen, F.; Dodelet, J.-P. Iron-Based Catalysts with Improved Oxygen Reduction Activity in Polymer Electrolyte Fuel Cells. *Science* **2009**, *324*, 71–74.
- (26) Wu, G.; More, K. L.; Johnston, C. M.; Zelenay, P. High-Performance Electrocatalysts for Oxygen Reduction Derived from Polyaniline, Iron, and Cobalt. *Science* **2011**, *332*, 443–447.
- (27) Wu, G.; Nelson, M. A.; Mack, N. H.; Ma, S.; Sekhar, P.; Garzon, F. H.; Zelenay, P. Titanium Dioxide-Supported Non-Precious Metal Oxygen Reduction Electrocatalyst. *Chem. Commun.* **2010**, *46*, 7489–7491.
- (28) Wu, G.; Mack, N. H.; Gao, W.; Ma, S.; Zhong, R.; Han, J.; Baldwin, J. K.; Zelenay, P. Nitrogen-Doped Graphene-Rich Catalysts Derived from Heteroatom Polymers for Oxygen-Reduction in Nonaqueous Lithium-O₂ Battery Cathodes. *ACS Nano* **2012**, *6*, 9764–9776.
- (29) Wu, G.; More, K. L.; Xu, P.; Wang, H.-L.; Ferrandon, M.; Kropf, A. J.; Myers, D. J.; Ma, S.; Johnston, C. M.; Zelenay, P. A Carbon-Nanotube-Supported Graphene-Rich Non-Precious Metal Oxygen Reduction Catalyst with Enhanced Performance Durability. *Chem. Commun.* **2013**, *49*, 3291–3293.
- (30) Lai, L.; Potts, J. R.; Zhan, D.; Wang, L.; Poh, C. K.; Tang, C.; Gong, H.; Shen, Z.; Lin, J.; Ruoff, R. S. Exploration of the Active Center Structure of Nitrogen-Doped Graphene-Based Catalysts for Oxygen Reduction Reaction. *Energy Environ. Sci.* **2012**, *5*, 7936–7942.
- (31) Wu, G.; Johnston, C. M.; Mack, N. H.; Artyushkova, K.; Ferrandon, M.; Nelson, M.; Lezama-Pacheco, J. S.; Conradson, S. D.; More, K. L.; Myers, D. J.; et al. Synthesis-Structure-Performance Correlation for Polyaniline-Me-C Non-Precious Metal Cathode Catalysts for Oxygen Reduction in Fuel Cells. *J. Mater. Chem.* **2011**, *21*, 11392–11405.
- (32) Figueiredo, J. L.; Pereira, M. F. R.; Freitas, M. M. A.; Orfao, J. J. M. Modification of the Surface Chemistry of Activated Carbons. *Carbon* **1999**, *37*, 1379–1389.
- (33) Sharifi, T.; Nitze, F.; Barzegar, H. R.; Tai, C.-W.; Mazurkiewicz, M.; Malolepszy, A.; Stobinski, L.; Waagberg, T. Nitrogen Doped Multi Walled Carbon Nanotubes Produced by CVD-Correlating XPS and Raman Spectroscopy for the Study of Nitrogen Inclusion. *Carbon* **2012**, *50*, 3535–3541.
- (34) Wu, G.; Nelson, M.; Ma, S.; Meng, H.; Cui, G.; Shen, P. K. Synthesis of Nitrogen-Doped Onion-Like Carbon and Its Use in Carbon-Based Cofe Binary Non-Precious-Metal Catalysts for Oxygen-Reduction. *Carbon* **2011**, *49*, 3972–3982.
- (35) Wu, G.; Li, D.; Dai, C.; Wang, D.; Li, N. Well-Dispersed High-Loading Pt Nanoparticles Supported by Shell-Core Nanostructured Carbon for Methanol Electrooxidation. *Langmuir* **2008**, *24*, 3566–3575.
- (36) Pylypenko, S.; Mukherjee, S.; Olson, T. S.; Atanassov, P. Non-Platinum Oxygen Reduction Electrocatalysts Based on Pyrolyzed Transition Metal Macrocycles. *Electrochim. Acta* **2008**, *53*, 7875–7883.
- (37) Artyushkova, K.; Pylypenko, S.; Olson, T. S.; Fulghum, J. E.; Atanassov, P. Predictive Modeling of Electrocatalyst Structure Based on Structure-to-Property Correlations of X-Ray Photoelectron Spectroscopic and Electrochemical Measurements. *Langmuir* **2008**, *24*, 9082–9088.
- (38) Ziegelbauer, J. M.; Olson, T. S.; Pylypenko, S.; Alamgir, F.; Jaye, C.; Atanassov, P.; Mukherjee, S. Direct Spectroscopic Observation of the Structural Origin of Peroxide Generation from Co-Based Pyrolyzed Porphyrins for ORR Applications. *J. Phys. Chem. C* **2008**, *112*, 8839–8849.
- (39) Xu, D.; Lu, P.; Dai, P.; Wang, H.; Ji, S. In Situ Synthesis of Multiwalled Carbon Nanotubes over LaNiO₃ as Support of Cobalt Nanoclusters Catalyst for Catalytic Applications. *J. Phys. Chem. C* **2012**, *116*, 3405–3413.
- (40) Qiao, J.; Xu, L.; Ding, L.; Zhang, L.; Baker, R.; Dai, X.; Zhang, J. Using Pyridine as Nitrogen-Rich Precursor to Synthesize Co-N-S/C Non-Noble Metal Electrocatalysts for Oxygen Reduction Reaction. *Appl. Catal., B* **2012**, *125*, 197–205.
- (41) Zheng, F.; Alayoglu, S.; Guo, J.; Pushkarev, V.; Li, Y.; Glans, P.-A.; Chen, J.-L.; Somorjai, G. In-Situ X-Ray Absorption Study of Evolution of Oxidation States and Structure of Cobalt in Co and CoPt Bimetallic Nanoparticles (4 nm) under Reducing (H₂) and Oxidizing (O₂) Environments. *Nano Lett.* **2011**, *11*, 847–853.
- (42) Wang, H. L.; Liang, Y. Y.; Gong, M.; Li, Y. G.; Chang, W.; Mefford, T.; Zhou, J. G.; Wang, J.; Regier, T.; Wei, F.; et al. An Ultrafast Nickel-Iron Battery from Strongly Coupled Inorganic Nanoparticle/Nanocarbon Hybrid Materials. *Nat. Commun.* **2012**, *3*, 1921/1–1921/8.
- (43) Liang, Y. Y.; Wang, H. L.; Diao, P.; Chang, W.; Hong, G. S.; Li, Y. G.; Gong, M.; Xie, L. M.; Zhou, J. G.; Wang, J.; et al. Oxygen Reduction Electrocatalyst Based on Strongly Coupled Cobalt Oxide Nanocrystals and Carbon Nanotubes. *J. Am. Chem. Soc.* **2012**, *134*, 15849–15857.
- (44) Leinweber, P.; Kruse, J.; Walley, F. L.; Gillespie, A.; Eckhardt, K. U.; Blyth, R. I. R.; Regier, T. Nitrogen K-Edge XANES - an Overview of Reference Compounds Used to Identify 'Unknown' Organic Nitrogen in Environmental Samples. *J. Synchrotron Radiat.* **2007**, *14*, 500–511.
- (45) Atribak, I.; Bueno-Lopez, A.; Garcia-Garcia, A. Uncatalysed and Catalysed Soot Combustion under NO_x + O₂: Real Diesel Versus Model Soots. *Combust. Flame* **2010**, *157*, 2086–2094.
- (46) Jung, H.-J.; Kim, B. W.; Abdul Malek, M.; Koo, Y. S.; Jung, J. H.; Son, Y.-S.; Kim, J.-C.; Kim, H. K.; Ro, C.-U. Chemical Speciation of Size-Segregated Floor Dusts and Airborne Magnetic Particles Collected at Underground Subway Stations in Seoul, Korea. *J. Hazard. Mater.* **2012**, *213*–214, 331–340.
- (47) Ferrari, A. C. Raman Spectroscopy of Graphene and Graphite: Disorder, Electron-Phonon Coupling, Doping and Nonadiabatic Effects. *Solid State Commun.* **2007**, *143*, 47–57.
- (48) Wu, G.; Swaidan, R.; Li, D.; Li, N. Enhanced Methanol Electro-oxidation Activity of PtRu Catalysts Supported on Heteroatom-Doped Carbon. *Electrochim. Acta* **2008**, *53*, 7622–7629.
- (49) He, Q.; Mukerjee, S.; Parres-Escapuez, S.; Bueno-Lopez, A. Effect of Praseodymium Oxide and Cerium-Praseodymium Mixed Oxide in the Pt Electrocatalyst Performance for the Oxygen Reduction Reaction in Pafcs. *J. Appl. Electrochem.* **2011**, *41*, 891–899.
- (50) He, Q.; Mugadza, T.; Hwang, G.; Nyokong, T. Mechanisms of Electrocatalysis of Oxygen Reduction by Metal Porphyrins in Trifluoromethane Sulfonic Acid Solution. *Int. J. Electrochem. Sci.* **2012**, *7*, 7045–7064.
- (51) Liang, Y. Y.; Li, Y. G.; Wang, H. L.; Zhou, J. G.; Wang, J.; Regier, T.; Dai, H. J. Co₃O₄ Nanocrystals on Graphene as a Synergistic Catalyst for Oxygen Reduction Reaction. *Nat. Mater.* **2011**, *10*, 780–786.
- (52) Liang, Y. Y.; Wang, H. L.; Zhou, J. G.; Li, Y. G.; Wang, J.; Regier, T.; Dai, H. J. Covalent Hybrid of Spinel Manganese-Cobalt Oxide and Graphene as Advanced Oxygen Reduction Electrocatalysts. *J. Am. Chem. Soc.* **2012**, *134*, 3517–3523.
- (53) Wang, H. L.; Liang, Y. Y.; Li, Y. G.; Dai, H. J. Co_{1-x}S-Graphene Hybrid: A High-Performance Metal Chalcogenide Electrocatalyst for Oxygen Reduction. *Angew. Chem., Int. Ed.* **2011**, *50*, 10969–10972.
- (54) Parvez, K.; Yang, S. B.; Hernandez, Y.; Winter, A.; Turchanin, A.; Feng, X. L.; Mullen, K. Nitrogen-Doped Graphene and Its Iron-Based Composite as Efficient Electrocatalysts for Oxygen Reduction Reaction. *ACS Nano* **2012**, *6*, 9541–9550.
- (55) Wu, Z. S.; Yang, S. B.; Sun, Y.; Parvez, K.; Feng, X. L.; Mullen, K. 3d Nitrogen-Doped Graphene Aerogel-Supported Fe₃O₄ Nanoparticles as Efficient Electrocatalysts for the Oxygen Reduction Reaction. *J. Am. Chem. Soc.* **2012**, *134*, 9082–9085.
- (56) Lin, Z. Y.; Waller, G.; Liu, Y.; Liu, M. L.; Wong, C. P. Facile Synthesis of Nitrogen-Doped Graphene via Pyrolysis of Graphene

Oxide and Urea, and Its Electrocatalytic Activity toward the Oxygen-Reduction Reaction. *Adv. Energy Mater.* **2012**, *2*, 884–888.

(57) Wu, G.; Dai, C.; Wang, D.; Li, D.; Li, N. Nitrogen-Doped Magnetic Onion-Like Carbon as Support for Pt Particles in a Hybrid Cathode Catalyst for Fuel Cells. *J. Mater. Chem.* **2010**, *20*, 3059–3068.

(58) Assumpcao, M. H. M. T.; Rascio, D. C.; Ladeia, J. P. B.; De Souza, R. F. B.; Teixeira Neto, E.; Calegari, M. L.; Oliveira, R. T. S.; Gaubeur, I.; Lanza, M. R. V.; Santos, M. C. Comparative Study of Different Methods for the Preparation of $\text{Co}_x\text{O}_y/\text{C}$ for the Electrosynthesis of Hydrogen Peroxide. *Int. J. Electrochem. Sci.* **2011**, *6*, 1586–1596.

(59) Hamdani, M.; Singh, R. N.; Chartier, P. Co_3O_4 and Co- Based Spinel Oxides Bifunctional Oxygen Electrodes. *Int. J. Electrochem. Sci.* **2010**, *5*, 556–577.

(60) He, Q.; Mukerjee, S.; Zeis, R.; Parres-Esclapez, S.; Illan-Gomez, M. J.; Bueno-Lopez, A. Enhanced Pt Stability in MO_2 ($\text{M} = \text{Ce}, \text{Zr}$ or $\text{Ce}_{0.9}\text{Zr}_{0.1}$)-Promoted Pt/C Electrocatalysts for Oxygen Reduction Reaction in PAFCs. *Appl. Catal., A* **2010**, *381*, 54–65.

(61) Sepa, D. B.; Vojnovic, M. V.; Damjanovic, A. Kinetics and Mechanism of O_2 Reduction at Pt in Alkaline Solutions. *Electrochim. Acta* **1980**, *25*, 1491–1496.

(62) Stamenković, V.; Schmidt, T. J.; Ross, P. N.; Markovic, N. M. Surface Composition Effects in Electrocatalysis: Kinetics of Oxygen Reduction on Well-Defined Pt_3Ni and Pt_3Co Alloy Surfaces. *J. Phys. Chem. B* **2002**, *106*, 11970–11979.

(63) Markovic, N. M.; Adzic, R. R.; Cahan, B. D.; Yeager, E. B. Structural Effects in Electrocatalysis: Oxygen Reduction on Platinum Low Index Single-Crystal Surfaces in Perchloric Acid Solutions. *J. Electroanal. Chem.* **1994**, *377*, 249–259.

(64) Lima, F. H. B.; Giz, M. J.; Ticianelli, E. A. Electrochemical Performance of Dispersed Pt-M ($\text{M} = \text{V}, \text{Cr}$ and Co) Nanoparticles for the Oxygen Reduction Electrocatalysis. *J. Braz. Chem. Soc.* **2005**, *16*, 328–336.

(65) Giacomini, M. T.; Ticianelli, E. A.; McBreen, J.; Salasubramanian, M. Oxygen Reduction on Supported Platinum/Polythiophene Electrocatalysts. *J. Electrochem. Soc.* **2001**, *148*, A323–A329.

(66) Markovic, N. M.; Schmidt, T. J.; Stamenkovic, V.; Ross, P. N. Oxygen Reduction Reaction on Pt and Pt Bimetallic Surfaces: A Selective Review. *Fuel Cells* **2001**, *1*, 105–116.

(67) Radyushkina, K. A.; Tarasevich, M. R. Chemisorption of Hydrogen and Oxygen on Dispersed Pt-Rh Powders. *Sov. Electrochem.* **1970**, *6*, 1627–1629.

(68) Lee, H.-J.; Choi, W. S.; Nguyen, T.; Lee, Y. B.; Lee, H. An Easy Method for Direct Metal Coordination Reaction on Unoxidized Single-Walled Carbon Nanotubes. *Carbon* **2011**, *49*, 5150–5157.

(69) Martell, A. E. Catalytic Effects of Metal Chelate Compounds. *Pure Appl. Chem.* **1968**, *17*, 129–178.

(70) Jaouen, F.; Proietti, E.; Lefevre, M.; Chenitz, R.; Dodelet, J.-P.; Wu, G.; Chung, H. T.; Johnston, C. M.; Zelenay, P. Recent Advances in Non-Precious Metal Catalysis for Oxygen-Reduction Reaction in Polymer Electrolyte Fuel Cells. *Energy Environ. Sci.* **2011**, *4*, 114–130.